Oxidation as Key Mechanism for Efficient Interface Passivation in $Cu(In,Ga)Se_2$ Thin-Film Solar Cells

Florian Werner,[1,*] Boris Veith-Wolf,[2] Conrad Spindler,[1] Michael R. Barget,[1,†] Finn Babbe,[1,‡] Jerome Guillot,[3] Jan Schmidt,[2,4] and Susanne Siebentritt[1]

[1] *Laboratory for Photovoltaics, Department of Physics and Materials Science, University of Luxembourg, 41 rue du Brill, L-4422 Belvaux, Luxembourg*

[2] *Institute for Solar Energy Research Hamelin (ISFH), Am Ohrberg 1, D-31860 Emmerthal, Germany*

[3] *Materials Research and Technology (MRT) Department, Luxembourg Institute of Science and Technology (LIST), 41 rue du Brill, L-4422 Belvaux, Luxembourg*

[4] *Department of Solar Energy, Institute of Solid-State Physics, Leibniz University Hannover, Appelstr. 2, D-30167 Hannover, Germany*

(Received 17 September 2019; revised manuscript received 17 March 2020; accepted 6 April 2020; published 4 May 2020)

Copper-indium-gallium-diselenide (CIGS) thin-film solar cells suffer from high recombination losses at the back contact and parasitic absorption in the front-contact layers. Dielectric passivation layers overcome these limitations and enable an efficient control over interface recombination, which becomes increasingly relevant as thin-film solar cells increase in efficiency and become thinner to reduce the consumption of precious resources. We present the optoelectronic and chemical interface properties of oxide-based passivation layers deposited by atomic layer deposition on CIGS. A suitable postdeposition annealing removes detrimental interface defects and leads to restructuring and oxidation of the CIGS surface. The optoelectronic interface properties are very similar for different passivation approaches, demonstrating that an efficient suppression of interface states is possible independent of the metal used in the passivating oxide. If aluminum oxide (Al_2O_3) is used as the passivation layer we confirm an additional field-effect passivation due to interface charges, resulting in an efficient interface passivation superior to that of a state-of-the-art cadmium-sulfide (CdS) buffer layer. Based on this chemical interface model we present a full-area rear-interface passivation layer without any contact patterning, resulting in a 1% absolute efficiency gain compared to a standard molybdenum back contact.

DOI: 10.1103/PhysRevApplied.13.054004

I. INTRODUCTION

Photovoltaic (PV) technologies directly convert sunlight into electricity and form a central part of a stable and clean energy supply based on renewable energy sources. For rapid deployment of PV at a global scale, material and energy consumption during solar-cell fabrication becomes an increasingly important factor to consider in addition to power-conversion efficiencies. While high-quality single-crystalline semiconductors historically have been most successful in terms of record efficiency [1], polycrystalline thin-film PV technologies use large-scale low-cost deposition processes [2], and were shown to have a lower environmental impact compared to their single-crystal counterparts, for example, in terms of energy payback time and carbon footprint [3–5]. Thin-film solar cells based on the ternary chalcopyrite $Cu(In,Ga)Se_2$ (CIGS) [6–8] are among the most efficient thin-film solar cells [1], having demonstrated efficiencies of 20.8% [9] on flexible and 22.3% [10] on rigid substrates (23.35% [11,12] with the addition of sulfur). Even the best devices still fall well short of the efficiency potential of ideal single-junction solar cells beyond 30% [13,14], and accurate understanding and effective suppression of nonradiative recombination losses is indispensable to bridge this efficiency gap.

Surfaces and interfaces potentially exhibit very high concentrations of recombination-active defect states: they represent areas of reduced crystal symmetry and disturbed chemical bonds, and they might be directly exposed to hostile environments—for example, a sputtering plasma—during device fabrication. Control over interface recombination is in fact a major challenge in CIGS

*fwerner.83@gmx.de

†Present address: STMicroelectronics, Agrate Brianza, Italy.

‡Present address: Lawrence Berkeley Laboratory, Berkeley, USA.

thin-film solar cells and severely limits device efficiency:

1. The conventional CdS buffer layer at the front junction between CIGS absorber and ZnO transparent contact ensures a good interface quality, but contains toxic Cd and causes high absorption losses due to its low bandgap [15].
2. The conventional Mo/CIGS back contact is highly defective with recombination velocities estimated to be larger than 10^5 cm/s [16].

In the field of *c*-Si photovoltaics, dielectric passivation layers at the front and rear surfaces of the silicon wafer are used with great success to suppress interface recombination [17–19]. Recent advances in perovskite and *c*-Si solar cells with carrier-selective contacts [19], which combine the functions of interface passivation and carrier extraction, furthermore prove that *p*-*n* junctions are not required for highly efficient devices.

Such alternative contacting concepts are also highly relevant for CIGS thin-film PV and open many opportunities to develop new front passivation approaches independent of the conventional CIGS/ZnO *p*-*n* heterojunction. In recent years, the concept of dielectric passivation layers has therefore been transferred from *c*-Si to CIGS solar cells [20–23]. Particularly aluminum oxide (Al_2O_3) deposited by atomic layer deposition [24] (ALD) has been established as the state-of-the-art passivation layer on *p*-type silicon surfaces [25–28]. Based on these experiences most studies also employ ALD-Al_2O_3 to passivate the *p*-type CIGS surfaces, with only a few studies focusing on alternative metal oxides, e.g., HfO_2, TiO_2, or SiO_2. Also other deposition techniques are used for *c*-Si, e.g., plasma-enhanced chemical vapor deposition [29,30] or rf sputtering [31], but ALD is particularly suited for applications in thin-film PV [17] due to the high surface roughness.

Promising improvements in open-circuit voltage and efficiency have been reported for CIGS solar cells with passivated rear contact and reduced absorber thickness [32]. Beneficial effects were also demonstrated at the front interface, where a thin layer of Al_2O_3 allows reduction of the CdS thickness [33]. Nevertheless, the knowledge of recombination processes at the Al_2O_3/CIGS interface remains largely limited to the device level, and its relation to interface chemistry, processing conditions, and postdeposition treatments is largely unexplored. The excellent passivation quality of Al_2O_3 on *c*-Si, for example, is due to a high negative fixed-charge density near the *c*-Si/Al_2O_3 interface, which results in a depletion of electrons from the passivated interface ("field-effect passivation") and a low interface defect density ("chemical passivation") [26,34]. These beneficial properties depend strongly on interface chemistry, which is very different between CIGS and Si. Furthermore, insulating dielectric passivation layers in polycrystalline CIGS devices require large-area patterning on a scale of a few tens of nanometers [35–37] to open conductive pathways, a factor of at least 1000 smaller than Si-PV, necessitating alternative approaches for industrial exploitation.

Thus, it is known in the literature, as presented in the preceding introduction, that high-quality interfaces between CIGS and Al_2O_3—and some other oxides as well—can significantly reduce recombination losses. Although this excellent interface passivation is attributed to a reduced interface state density and field-effect passivation due to fixed charges potentially located within the Al_2O_3 layer, the exact mechanisms behind these passivation effects are unexplored. There is also substantial uncertainty regarding which processing conditions a good interface passivation can be achieved under, which factors affect long-term stability, and how dielectric passivation layers can best be incorporated in a simple scalable solar-cell fabrication process. These questions are best addressed by combining optoelectronic characterization of test devices and solar cells with chemical analysis of the interfacial region between CIGS and passivation layer. In this paper we combine photoluminescence (PL), admittance spectroscopy, and x-ray photoelectron spectroscopy (XPS) to quantify recombination losses and study the effect of a postdeposition annealing process on CIGS thin films passivated with ALD-Al_2O_3. We find that annealing is required to recover interface damage (Sec. III). Passivation of electronic interface states in CIGS can be understood by alkali accumulation and the growth of an interfacial indium-gallium-oxide interlayer during annealing (Sec. IV). Chemical passivation is driven by oxidation and independent of the actual metal constituent of the passivation layer, but field-effect passivation due to negative fixed charges is specific to Al_2O_3 annealed at sufficiently high temperatures (Sec. V). Based on these observations we propose a full-area compact passivation layer of TiO_2 at the rear interface between Mo back contact and CIGS absorber. Without any contact patterning we demonstrate an efficiency enhancement by 1% absolute on a thin ungraded CIGS proof-of-concept device (Sec. VI).

Our findings provide key perspectives to interface passivation in CIGS solar cells:

1. It is mostly the oxygen that provides a large part of the beneficial effect of Al_2O_3—or other oxide-based dielectric passivation layers—meaning that the actual material used for the passivation layer is less relevant.
2. Contact patterning is not required, and full-area passivation layers provide an efficiency boost with a very simple device process.

II. METHODS

Device fabrication: Cu-poor CIGS thin-film absorbers with a thickness of approximately 2 μm are deposited

by co-evaporation on Mo-coated soda-lime glass (SLG) in a three-stage process. The average elemental composition as determined by energy dispersive x ray (EDX) corresponds to CGI = [Cu]/([Ga] + [In]) = 0.87–0.98 and GGI = [Ga]/([Ga] + [In]) = 0.22–0.30, and is thus representative of typical state-of-the-art CIGS solar-cell devices. Reference solar cells fabricated from substrates processed in the same deposition runs achieve power-conversion efficiencies of 16%–18% under standard testing conditions, confirming a good electronic quality. Note that no alkali postdeposition treatment has been applied to any of these devices. The absorber films are etched in a 5 wt-% aqueous solution of potassium cyanide (KCN) to remove surface contaminations, immediately sealed in a vacuum bag and shipped to the Institute for Solar Energy Research Hamelin (ISFH) for ALD. Some samples instead receive a CdS buffer layer (thickness estimated from typical growth rates: 40–50 nm) deposited by chemical bath deposition, representative of the CIGS/CdS interface in state-of-the-art solar cells. Circular Au contacts with 1 mm diameter are evaporated by electron-beam evaporation through a shadow mask to form a metal-insulator-semiconductor (*M-I-S*) structure for electrical measurements.

Amorphous Al_2O_3 is deposited by plasma-assisted ALD using trimethyl-aluminum [TMA, $[Al(CH_3)_3]_2$] as aluminum precursor and oxygen radicals generated in an inductively coupled remote oxygen plasma for oxidation. The substrate temperature is limited to 130 °C to avoid any potential loss of selenium from the CIGS absorber. Test devices processed from lowly doped float-zone *c*-Si wafers achieved very low maximum effective surface-recombination velocities below 2.5 cm/s (assuming an infinite bulk lifetime) despite the low deposition temperature.

Temperature-dependent capacitance measurements are performed in a closed-cycle cryostat in the dark. The sample temperature is measured with a Si-diode sensor glued onto an identical glass substrate beside the *M-I-S* device. Conductance and capacitance are measured with an *LCR* meter (frequency range: 20 Hz–2 MHz, ac voltage amplitude: 30 mV rms) assuming a standard parallel equivalent circuit model. For voltage-dependent measurements we monitor the actual dc voltage across the terminals of the *M-I-S* device to account for the internal resistance of the *LCR* meter.

For **calibrated PL measurements**, the Al_2O_3/CIGS samples are excited by a diode laser at a wavelength of 633 nm at room temperature and the emitted PL is recorded by an (In, Ga)As photodiode array detector. Spectral correction is applied using a calibrated halogen lamp. The beam diameter and laser power are measured with a charge-coupled device camera and power meter, respectively, to calibrate the photon flux. Time-resolved PL (TRPL) measurements are performed with a pulsed laser diode at 638-nm wavelength and 100-ps pulse width. The PL transients are recorded with a time resolution of approximately 400 ps with a near-infrared photomultiplier tube employing time-correlated single-photon counting.

Thermal annealing is performed inside a graphite box in a rapid thermal processing (RTP) tool with a background pressure of 800 mbar of nitrogen. A thermocouple probing the temperature of the graphite box is used to control the process.

XPS measurements are performed with monochromatic Al K_α illumination under 0° emission angle with respect to surface normal. The analyzed area is approximately $700 \times 300\ \mu m^2$, the energy resolution is 0.5 eV (pass energy: 20 eV). No charge compensation or energy calibration is performed for most spectra (Se 3*d* spectra are calibrated with C 1s at 285.0 eV).

Solar-cell parameters are measured by current-voltage measurements with a class AAA solar simulator. External quantum efficiency (EQE) is measured using chopped illumination from a halogen-xenon lamp and a lock-in amplifier to measure the photocurrent.

III. INTERFACE PASSIVATION AND THE ROLE OF THERMAL ANNEALING

We use Al_2O_3 layers of nominally 20 nm (180 ALD cycles) deposited by plasma-assisted ALD as the baseline for the study of interface recombination at Al_2O_3-passivated CIGS surfaces. We obtain qualitatively similar trends also for subnanometer thick Al_2O_3 films, but capacitance measurements on such devices are less precise due to the higher leakage currents. Note that we use the stoichiometric formula "Al_2O_3" instead of "AlO_x" to describe aluminum oxide layers deposited by ALD, which are expected to be highly uniform and stoichiometric, although the actual elemental composition is likely different close to the initial growth interface [34].

A. Effect of temperature on recombination losses

It is well known for *c*-Si solar cells that plasma-assisted ALD of Al_2O_3 initially results in a very poor surface quality and requires a thermal-annealing process to effectively "activate" the interface passivation: the characteristic features of well-passivating Al_2O_3—a high negative fixed-charge density and low interface trap density—are shown to only form during a thermal postdeposition anneal [38]. Even for mild deposition processes, e.g., thermal ALD using short water-vapor pulses instead of oxygen plasma, a postdeposition anneal significantly improves the interface passivation quality and increases the effective carrier lifetime [39,40]. We observe the same effect also for Al_2O_3 deposited on CIGS, in agreement with earlier reports [41] that suggest thermal postdeposition treatments can be beneficial also for Al_2O_3-passivated CIGS.

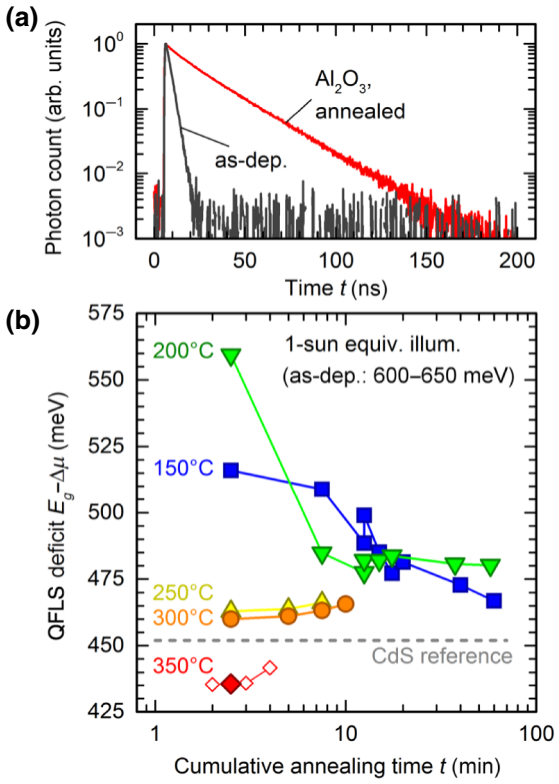

FIG. 1. Effect of annealing on recombination losses. (a) Normalized TRPL measurements of a CIGS absorber coated with 20 nm of Al_2O_3: as-deposited (gray line) and annealed for 2 min at 350 °C (red line). Background signal measured without excitation is subtracted. (b) Quasi-Fermi-level-splitting deficit measured under 1-sun equivalent illumination for different annealing times and temperatures (solid symbols). Open symbols for 350 °C are noncalibrated PL measurements scaled to match the calibrated measurement at 2.5 min. As-deposited devices (QFLS deficit approximately equals 600–650 meV) are off the chart, the QFLS deficit of 451 meV for a reference device with CdS buffer layer (no annealing) is indicated by the gray dashed line.

Figure 1(a) shows TRPL measurements of a CIGS absorber covered with 20 nm of Al_2O_3 in the as-deposited state (gray line) and after annealing the sample for 2 min at 350 °C (red line). The initially low effective lifetime below 3 ns increases by one order of magnitude to 25 ns upon annealing.

The quasi-Fermi-level splitting (QFLS) $\Delta\mu$ of the passivated CIGS absorber layer is readily accessible by calibrated PL measurements [42] and provides an upper limit for the open-circuit voltage V_{OC} potential in a full solar cell, without requiring any device processing (e.g., contact patterning) after depositing the passivation layer. For devices based on CIGS it is more appropriate to compare the QFLS *deficit*, i.e., the difference $E_g - \Delta\mu$ between bandgap and QFLS: the bandgap directly affects the QFLS, and in the case of CIGS varies even with small fluctuations in elemental composition. Indeed, the energy of the PL peak maximum, which we use as an indicator of the bandgap energy, differs by 70 meV between different absorber films. The QFLS *deficit* is a measure of the recombination *losses*, and thus low values of the QFLS deficit are beneficial.

Figure 1(b) shows the QFLS deficit at an equivalent illumination of 1 sun (laser photon flux set equal to the absorbed photon flux under 100 mW/cm^2 AM1.5G) after successive annealing in nitrogen ambient at different temperatures. The as-deposited QFLS deficit after ALD is in a range of 600–650 meV, comparable to values measured on bare CIGS surfaces degraded after storage. As-deposited Al_2O_3 obviously results in a very poor interface quality and high recombination losses, in good agreement with the low initial lifetimes observed in TRPL. After annealing, recombination losses and the corresponding QFLS deficit decrease drastically. For moderate annealing temperatures in a range of 150–300 °C the QFLS deficit can be reduced to values around 460–480 meV. Although this is an improvement of more than 100 meV compared to the as-deposited case, it cannot compete with a state-of-the-art CdS buffer layer deposited by chemical bath deposition [451 meV, gray line in Fig. 1(b)].

At the highest annealing temperature of 350 °C, Al_2O_3 achieves a QFLS deficit as low as 435 meV and thus almost 20 meV better than CdS. As we discuss below, the reason for this marked improvement at 350 °C is a field-effect passivation due to the formation of negative fixed charges in the Al_2O_3 passivation layer, which are absent at lower annealing temperatures.

Interface passivation with an Al_2O_3 layer on CIGS is stable over long time periods. Samples have been stored in evacuated plastic bags and remeasured after 1 year, where we find essentially the same PL lifetime and QFLS deficit as before. For the best sample annealed for 2.5 min at 350 °C, for example, we measure a QFLS deficit of 424 meV after one year compared to the initial 435 meV. This difference of the order of 10 meV is not significant taking into account that both measurements are performed with different laser calibrations one year apart.

We conclude that Al_2O_3 deposited by ALD onto CIGS can passivate the interface as well as state-of-the-art CdS or even better, but a suitable postdeposition annealing is mandatory. Surprisingly, the thermal budget required to achieve an excellent interface passivation is much lower for CIGS than for *c*-Si: annealing for only 2–3 min at 350 °C is already sufficient in the case of CIGS/Al_2O_3, while an optimal annealing process in the case of *c*-Si/Al_2O_3 requires around 15 min at temperatures of 400 °C or 30 min at 350 °C [38]. Faster timescales during annealing can also play a crucial role for the thermal stability of passivation layers during device fabrication: at temperatures around 250–300 °C we observe only a very minor deterioration of the QFLS with annealing duration beyond the optimum, but this degradation is clearly

visible at 350 °C for annealing times longer than 3 min. Importantly, degradation occurs only during excessive annealing, during room-temperature storage the interface quality remains stable.

Note that initial experiments with annealing temperatures of 400 °C, albeit for a nonoptimized ALD process, result in poor lifetimes around 1–5 ns, presumably due to severe degradation. We thus do not carry out systematic experiments at annealing temperatures above 350 °C.

B. Interface defects

Enhanced PL lifetime and QFLS after annealing indicate a reduction of detrimental recombination channels in the device. One evident candidate for such an improvement is a reduction of recombination-active defect states at the CIGS/Al_2O_3 interface during annealing, which we verify by electrical measurements on Au/Al_2O_3/CIGS *M-I-S* devices.

Defects at the interfaces or in the bulk of a semiconductor device can be identified from characteristic steps in the capacitance spectrum of a solar cell or *M-I-S* device [43,44]. We compare capacitance spectra of as-deposited devices and devices annealed for 2.5 min at 350 °C to quantify the reduction of interface defects by an annealing process.

Experimental capacitance spectra (see Fig. S1 within the Supplemental Material [45]) clearly show one dominant capacitance step before and after annealing, but the origin of these steps is not the same, as revealed by the voltage dependence of the defect activation energy shown in Fig. 2.

For the as-deposited device, the activation energy of the dominant capacitance step increases linearly in reverse bias. This behavior is characteristic for a continuous distribution of interface traps, as sketched in the inset of Fig. 2, where the activation energy changes with band bending in the space-charge region (SCR). The voltage-dependent activation energy calculated for such an interface-defect distribution is illustrated by the red line in Fig. 2, where material parameters are chosen to best fit the experimental data (net doping $N_a = 8 \times 10^{16}$ cm^{-3}, interface trap density $D_{IT} = 1.2 \times 10^{12}$ eV^{-1} cm^{-2}, oxide capacitance $C_{ox} = 290$ nF/cm^2, flatband voltage $V_{FB} = 650$ mV) and are consistent with independent electrical measurements [46–50] (see Sec. B within the Supplemental Material [45] for a comparison). Interface trap densities calculated from the conductance peak height or capacitance step height [44], for example, both yield values around $(1–2) \times 10^{12}$ eV^{-1} cm^{-2}. In forward bias, the dominant capacitance step of the as-deposited device is best described by two independent activation energies at high and low temperatures (see Fig. S1 within the Supplemental Material [45]; open and closed circles in Fig. 2, respectively). We attribute this effect to an overlap between two distinct capacitance steps, which we cannot resolve individually.

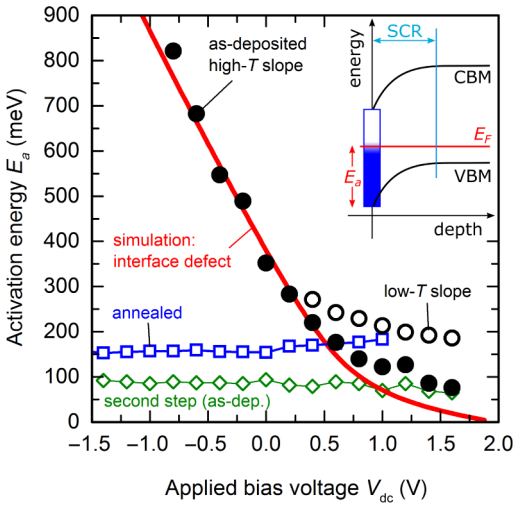

FIG. 2. Interface defects in admittance spectroscopy. Activation energies E_a obtained from temperature-dependent inflection frequencies as a function of applied dc bias voltage V_{dc} for an as-deposited sample (black circles, closed/open symbols correspond to different slopes at high and low temperatures) and a device annealed for 150 s at 350 °C (blue squares). Green diamonds represent a second capacitance feature between 19–25 nF/cm^2 barely visible in the as-deposited sample. The solid red line is a calculation based on material parameters chosen to best fit the data (see text). Inset: sketch of the conduction-band minimum (CBM), valence-band maximum (VBM), and majority carrier Fermi level E_F at an insulator-semiconductor interface. The box outlined in blue represents a continuous distribution of interface trap states, with their occupation shown in blue.

The device annealed at 350 °C shows no evidence of interface defects: the dominant capacitance step corresponds to a voltage-independent activation energy of 175 ± 25 meV across the full experimental voltage range. For a discreet bulk defect level, the energetic separation between trap level and majority carrier band edge indeed remains constant independent of band bending. The activation energy around 175 meV agrees remarkably well with the "low-temperature" activation energy of the as-deposited sample in forward bias.

We conclude that the capacitance response of the as-deposited sample is dominated by interface traps, but is actually given by the superposition of (i) the voltage-dependent activation energy identified with a continuous distribution of interface trap states at the Al_2O_3/CIGS interface and (ii) a discrete trap level around 175 meV. After a suitable annealing process, e.g., 150 s at 350 °C, trap states at the interface are effectively removed and only the constant 175 meV level remains. The nature of this 175 mV level might be related to selenium defects and is discussed in Sec. V D.

Suitable thermal annealing thus successfully removes interface defects present after deposition of the Al_2O_3 passivation layer by ALD. Without postdeposition annealing,

these interface trap states cause strong nonradiative recombination and dominate the device response in electrical characterization.

C. Formation of fixed charges at the Al_2O_3/CIGS interface

A reduction of interface defects is not the only approach to suppress interface recombination. As discussed in the introduction, fixed charges in the passivation layer can lead to a relative depletion of one carrier type in the absorber (electrons for negative fixed charge, holes for positive fixed charge), thereby creating a "field-effect passivation" because recombination rate is roughly proportional to the product of electron and hole concentration at the interface.

Al_2O_3 is particularly promising for the passivation of p-type semiconductors, like CIGS, because a high density of negative fixed interface charges is expected to form upon annealing, resulting in an effective field-effect passivation. The total interface-charge density $Q = Q_f + Q_{IT}$, which is the sum of fixed charge Q_f and defect-trapped charge Q_{IT} at the interface, can be calculated [44] from the flatband voltage accessible in a capacitance measurement. With some reasonable assumptions (bulk Fermi level $E_F = 150$ meV, Au work function $W_{Au} = 5.1$, CIGS electron affinity $\chi_{CIGS} = 4.35$), both experiment and simulation shown in Fig. 2 for the as-deposited device correspond to a total *positive* interface-charge density of $Q \approx +5 \times 10^{11}$ cm^{-2}. This value is of the order of the interface trap density, and an accurate value of the fixed-charge density cannot be stated because only the sum of Q_f and Q_{IT} is known. If we assume that interface defects are acceptorlike below midgap and donorlike above midgap, $Q_{IT} \approx +5 \times 10^{11}$ cm^{-2} and thus $Q_f \approx 0$ for as-deposited Al_2O_3 on CIGS.

The impact of annealing on the interface trap and charge densities can be seen in the capacitance-voltage (CV) relations shown in Fig. 3 for three different annealing processes: as-deposited (no annealing, black circles), a long low-temperature anneal (60 min at 150 °C, blue squares), and the optimum annealing process (2.5 min at 350 °C, red diamonds). A steeper curve corresponds to a reduced defect density, and a shift along the voltage axis in positive or negative direction corresponds to a positive or negative interface-charge density: for the given Al_2O_3 thickness, a shift of 1 V corresponds to $(1.8 \pm 0.1) \times 10^{12}$ cm^{-2} unit charges, see Eq. (S2) within the Supplemental Material [45]. At the lower annealing temperature of 150 °C, interface trap states are mostly passivated after 1 h of annealing, but there is no evidence for the formation of fixed charges, which could provide a field-effect passivation. Accordingly, the QFLS deficit after annealing for 60 min at 150 °C remains inferior to the CdS-covered reference sample (see Fig. 1).

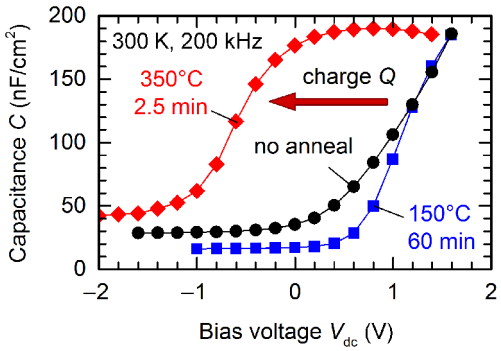

FIG. 3. Fixed interface-charge formation. Capacitance-voltage characteristics $C(V_{dc})$ at $T = 300$ K and $f = 200$ kHz of a Au/Al_2O_3/CIGS M-I-S device with 20 nm Al_2O_3 after different annealing procedures in nitrogen ambient: no annealing (black circles), 60 min at 150 °C (blue squares), and 2.5 min at 350 °C (red diamonds).

Optimal annealing conditions of 2.5 min at 350 °C evidently lead to the formation of negative fixed interface charges of $-(2 \pm 1) \times 10^{12}$ cm^{-2}, as seen from the voltage shift of the corresponding CV profile in Fig. 3. The resulting field-effect passivation explains the reduced recombination losses at the interface and the correspondingly low QFLS deficit of 435 meV.

Exceeding a certain annealing temperature appears to be more important than the total thermal budget for the formation of negative interface charges: annealing at 300 °C results in a comparable interface passivation as 150 °C, only the timescales required for optimum annealing are shorter (a few minutes compared to one hour). Fixed charges do not form even after 10 min of annealing. Apparently, a minimum annealing temperature above 300 °C is required for our absorber process to create negative fixed interface charges in the passivation layer. Although we expect this trend to hold for any typical CIGS absorbers, the exact annealing conditions required for optimum passivation performance might be different for other absorber growth conditions or passivation-layer deposition processes.

IV. CHANGES IN CHEMICAL COMPOSITION AT THE INTERFACE DURING ANNEALING

To understand the mechanisms of defect removal and fixed-charge formation, it is necessary to correlate changes in optoelectronic properties to modifications in interface chemistry. We use SIMS and XPS to study compositional changes and changes in chemical bonds at the Al_2O_3/CIGS interface upon annealing. Since XPS is a very surface-sensitive technique, the Al_2O_3 films for these measurements are only approximately 0.5 and 1.0 nm thin to obtain enough signal from Al_2O_3, interfacial region, and underlying CIGS in a single measurement. We compare

three different annealing conditions: as-deposited, 20 min at 150 °C (low temperature), and 150 s at 350 °C (high temperature). For the low-temperature annealing, the photoelectron spectra remain mostly unchanged, except for minor variations in carbon contamination. Upon high-temperature annealing, however, we observe significant changes in the chemical environment around the interface, as described below.

Sodium (Na) is highly mobile in CIGS, in particular at elevated temperatures during annealing, and is known to affect device efficiency and electronic defect properties [51–53]. It is also known to interact with oxygen, potentially catalyzing surface oxidation of CIGS [54]. Figure 4(a) shows the Na 1s core-level peak recorded by XPS at a binding energy close to 1072 eV [55] for Al_2O_3-covered CIGS (solid lines) and a bare CIGS film freshly etched in KCN (dashed line). Depth profiles of the Na concentration around the Al_2O_3/CIGS interface measured by SIMS before and after high-temperature annealing are shown in Fig. 4(b). For SIMS measurements, the Al_2O_3 is 20 nm thick. Depth profiles for oxygen (from Al_2O_3) and selenium (from CIGS) are shown in gray—scaled to similar intensity—to indicate the physical location of the Al_2O_3/CIGS interface. The annealing process clearly leads to a pronounced accumulation of Na directly at the interface, which could help to saturate fractured bonds at the interface and thus reduce the interface state density. The large supply of Na from the SLG substrate and its high mobility in CIGS then result in a fast and efficient chemical passivation of interface defects, which could explain the short annealing times sufficient to significantly reduce interface trap concentration. A similar process has been observed for the passivation of *c*-Si surfaces, where atomic hydrogen supplied by the passivation layer migrates to the interface and saturates Si dangling bonds [38,56]. The fabrication process also supplies K from the SLG in addition to Na, but the response to thermal annealing is different in the case of K (see Fig. S2 within the Supplemental Material [45]): although K also accumulates at the interface, this is already the case for the as-deposited sample and does not change much during annealing. Accordingly, K is unlikely to play a major role in interface passivation.

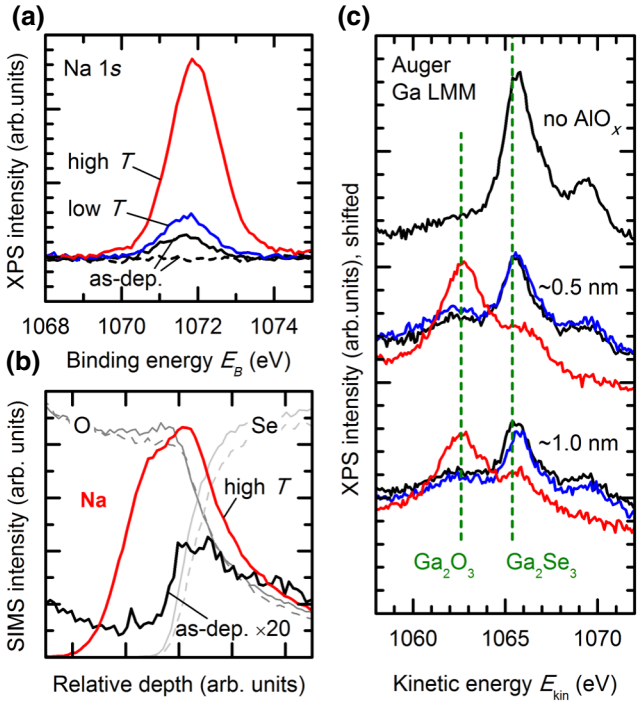

FIG. 4. Evolution of chemical composition for different annealing conditions: as-deposited (black lines), 20 min at 150 °C (blue lines), and 150 s at 350 °C (red lines). (a) Na 1*s* core-level XPS peak for samples with approximately 0.5 nm Al_2O_3 (solid lines) and a bare CIGS reference freshly etched in KCN (dashed line). Background signal subtracted for clarity. (b) SIMS depth profile of Na around the interface between Al_2O_3 and CIGS (as-deposited Na signal magnified by ×20). Normalized oxygen and selenium signals are shown in gray (solid, as-deposited; dashed, annealed) to mark the interface. (c) Ga LMM Auger peak of bare CIGS (top) and CIGS covered with 0.5 nm (middle) and 1.0 nm (bottom) of Al_2O_3 (data shifted vertically for clarity). Literature values [51] for Ga_2O_3 and Ga_2Se_3 are indicated in the graph.

While Na migration can potentially explain chemical passivation of defect states, it cannot be the only effect of an annealing process: Na will always be neutral or positively charged, and migration of Na^+ ions to the interface cannot explain the formation of a substantial *negative* interface-charge density. In the following we focus on chemical changes of the intrinsic elements Cu, In, Ga, and Se upon annealing.

The chemical environment of Cu remains unchanged during the annealing process (see Fig. S2 within the Supplemental Material [45]), with a measured Auger parameter of 1849.3–1849.5 eV for all seven samples, values typical for Cu in a $CuInSe_2$-like structure [57,58]. After high-temperature annealing, the integrated intensity of the Cu-related peaks however decreases, indicating a Cu depletion near the interface. Such a Cu redistribution has previously been observed for bare CIGS absorbers annealed in air [59], where oxidation was found to remove Cu from the interface and to also reduce interface defects causes by Se deficiency.

For the group-III elements In and Ga, we observe negligible changes during the low-temperature annealing, but significant oxidation after high-temperature annealing. This trend is most clearly seen in the Ga LMM Auger peak shown in Fig. 4(c), which shifts by almost 3 eV from 1065.7 to 1063.0 eV after high-temperature annealing. This change is best explained by a shift from a Ga_2Se_3-like environment (Ga_2Se_3 literature: 1065.4 eV [60], our data: 1065.7 eV) to a Ga_2O_3-like environment (Ga_2O_3 literature: 1062.6 eV [60], our data: 1063.0 eV). As can be seen in

Fig. 4(c), a substantial fraction of Ga within the detection volume is oxidized for both thicknesses (approximately 0.5 and 1.0 nm) of Al_2O_3. Furthermore, as expected, the ALD process itself already results in a slight interface oxidation in the as-deposited samples. Such initial oxidation is mostly absent in the bare reference sample, see the top curve in Fig. 4(c), which had been etched in KCN shortly before the XPS measurement in order to remove such residual oxides.

Reconstructions of the Se 3*d* peak shown in Fig. 5 for different annealing conditions confirm the appearance of an oxidized interlayer between the initial Al_2O_3 and CIGS upon high-temperature annealing. Beyond the main CIGS peak "Se-1" at 54.0 eV [61] (gray), Al_2O_3-covered CIGS shows two additional chemical states of Se, which are absent in the bare (etched) reference: one around 59 eV (green), which can be attributed to SeO_2 [55], and a contribution "Se-2" around 55 eV (red), which we tentatively attribute to a mixed oxide, presumably $Cu(In,Ga)Se_xO_y$. The amount of this secondary mixed selenium oxide Se-2 increases notably upon high-temperature annealing. At the same time, the integrated Se signal decreases. Note that this agrees with the SIMS profiles shown in Fig. 4(b), where the onset of the Se signal in the annealed sample (dashed line) shows a slight shift relative to the as-deposited sample (solid line). In addition to the formation of this mixed selenide oxide, the disappearance of Cu and Se from the initial Al_2O_3/CIGS interface suggests the growth of an interfacial $(In,Ga)O_x$ layer as sketched in Fig. 6(a).

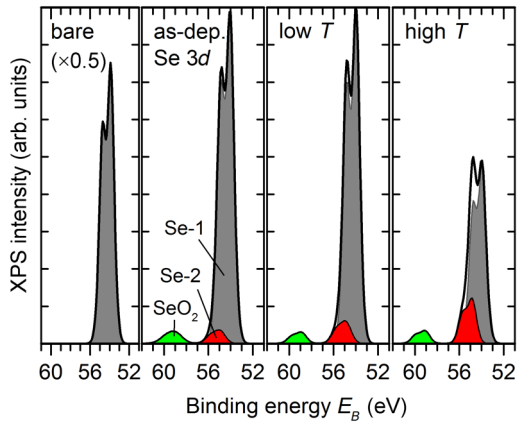

FIG. 5. Oxidation of selenium. Reconstruction of the Se 3*d* core-level XPS peak (solid black line) of a bare KCN-etched CIGS absorber (very left, scaled by 1/2) and three absorbers with 1 nm AlO_x: as-deposited (left), low-temperature (middle, 20 min at 150 °C), and high-temperature anneal (right, 150 s at 350 °C) with three contributions: Se-1 attributed to chalcopyrite (gray), Se-2 attributed to a mixed oxide (red), and SeO_2 (green). The doublet peak shape originates from the spin-orbit splitting between $3d_{3/2}$ and $3d_{5/2}$. The trend is the same for 0.5 nm of AlO_x.

V. KEY MECHANISMS OF SURFACE PASSIVATION IN CIGS

A. Surface damage during ALD

Without suitable postdeposition annealing, Al_2O_3 deposited onto CIGS by plasma-assisted ALD does not provide any benefit concerning the passivation of electronic surface defects. We find that this also applies to Al_2O_3 or TiO_2 deposited by thermal ALD (see Fig. S3 within the Supplemental Material [45]). Nonradiative recombination at such interfaces is high, which we find to originate from a high concentration of electronic interface traps distributed throughout the CIGS bandgap. We are unable to identify the particular physico-chemical origin for this interface defect distribution. Plasma damage from the plasma-assisted ALD process appears unlikely, because thermal ALD using water vapor instead of the oxygen plasma results in similar interface-state distributions and correspondingly high interface recombination in the as-deposited state.

Oxygen might be a candidate to explain a degradation of the CIGS surface during the ALD process. There appears to be no clear consensus whether surface oxidation of CIGS is beneficial or detrimental, and evidently both cases occur depending on the exact oxidation mechanism: native oxidation had been demonstrated and linked to degradation for bare CIGS surfaces [62–64], but oxidation at elevated temperatures passivates defects (see discussion below and Ref. [59]). We indeed confirm significant changes of the interface-near CIGS composition due to oxidation already during the ALD process, as for example shown by the Ga and Se peaks of the as-deposited sample in Figs. 4 and 5. These changes, however, become increasingly prominent with thermal annealing, while—at the same time—the interface-state density decreases. Accordingly, interface states in the as-deposited sample are presumably not related to oxidation, but most likely must be attributed to structural defects caused by an initially nonideal growth of the oxide layer on CIGS, an effect already observed for ALD of Al_2O_3 on *c*-Si [34].

B. Interface oxidation

No matter the microscopic origin of the poor as-deposited performance, a suitable annealing treatment reduces the high interface-state density and thereby suppresses nonradiative recombination. Compared to *c*-Si devices, this annealing is effective already at significantly shorter annealing durations. Studies of the chemical composition mostly showed changes at the Al_2O_3/CIGS interface and within the top surface-near layer of CIGS:

1. Alkali atoms—mostly Na—accumulate at the interface even for low thermal budgets during annealing. This could result in a passivation of dangling bond defects, similar to hydrogen passivation in *c*-Si.

2. Even for as-deposited Al_2O_3 on CIGS, the Se-related XPS peaks show contributions from Se oxides. Most notably, the signal attributed to a mixed oxide selenide, presumably $Cu(In,Ga)Se_xO_y$, increases upon annealing. This feature shows the strongest correlation to the reduced interface-state density, and thus must be considered a prime candidate to understand passivation of interface defects.

3. At high annealing temperatures, Cu and Se are depleted from a thin layer of (formerly) CIGS at the CIGS/Al_2O_3 interface. This results in the growth of a layer of group-III oxides between CIGS and Al_2O_3.

These three effects relate to the CIGS absorber itself, in particular to a thin region just below the interface to the passivation layer. Figure 6(a) depicts a model of the different interlayers forming during a high-temperature anneal. Most likely interfaces between the different compositions will not be well defined, resulting in a more-or-less smooth transition along Al_2O_3 → III oxides → III oxide selenides → CIGS. In this model, interface oxidation during annealing plays a key role in suppressing recombination losses at the CIGS-passivation interface. That observation could mean that the actual nature of the passivation layer might be irrelevant, as long as it promotes oxidation of the underlying CIGS.

We compare different oxide-based passivation schemes to verify whether Al_2O_3 has any specific function in interface passivation. Figure 6(b) shows the QFLS deficit

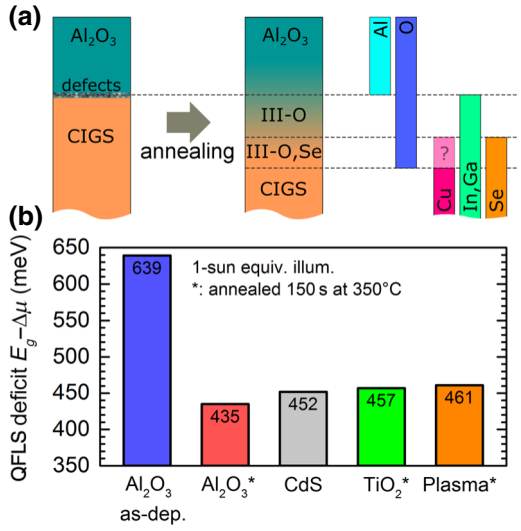

FIG. 6. Interface model. (a) Sketch of elemental depth profiles and chemical environment of the as-deposited (left) and high-temperature annealed (right) Al_2O_3/CIGS interface. (b) Quasi-Fermi-level-splitting deficit $E_g - \Delta\mu$ for CIGS passivated with: Al_2O_3 (same data as Fig. 1), standard CdS buffer layer, TiO_2, and exposed to the oxygen plasma in the ALD reactor. Except for as-deposited Al_2O_3 and CdS, all samples are annealed for 150s at 350 °C.

$E_g - \Delta\mu$ for CIGS covered with Al_2O_3 (as-deposited, blue bar; optimum anneal, red bar) and a standard CdS buffer layer deposited by chemical bath deposition (gray bar). We compare this data to the QFLS deficit of CIGS passivated with a thin layer of amorphous TiO_2 deposited by thermal ALD (30 ALD cycles, approximately 2 nm, same annealing conditions as Al_2O_3), which results in a passivation quality comparable to CdS. Going one step further, we expose the surface of a CIGS absorber film to 50 cycles of oxygen plasma within the ALD chamber, keeping all precursor lines except oxygen closed (i.e., no metals are deposited). After annealing the QFLS deficit reaches values around 460 meV and thus again very similar to CdS. Despite the excellent performance after annealing, all samples—except CdS—show very high QFLS deficits before annealing (not shown here), independent of whether water vapor (in thermal ALD) or oxygen plasma (in plasma-assisted ALD) is used as the oxygen source. Thus, the mere presence of oxygen is not sufficient to guarantee a low interface recombination velocity, but rather appears to be detrimental at least in the ALD processes presented here. A beneficial effect of these oxide-based passivation schemes only manifests after an appropriate thermal-annealing process, after which QFLS deficits very similar to state-of-the-art CdS can be achieved. This confirms that the actual chemical nature of the passivation layer itself is less important, as long as it provides the oxygen for a controlled oxidation of the CIGS surface. Even exposure to an oxygen plasma—without any actual passivation layer being deposited—is sufficient to achieve a remarkably low QFLS deficit after annealing. In fact, after annealing, surface recombination at such a plasma-exposed CIGS surface is suppressed to values very comparable to a TiO_2 passivation layer or CdS buffer layer.

The previous experiments cannot distinguish whether interface passivation is indeed a consequence of CIGS interface oxidation, or simple due to the annealing process itself. We do not have a truly oxygen-free control sample to answer this question: our experimental setup requires short exposure to air between experiments, and chemical etching of oxide contaminations could lead to oxidation of the CIGS surface as well. Nevertheless, we compare one as-grown CIGS absorber and one freshly etched in a 5 wt-% KCN solution before and after annealing for 2.5 min at 350 °C in nitrogen gas, as shown in Fig. 7. In both cases, annealing leads to a degradation of interface quality and increases recombination losses. Accordingly, we find that annealing alone—without adequate supply of oxygen—has no beneficial effect for our devices.

C. Fixed-charge density

Despite our observation that the material of the passivation layer is of secondary concern in relation to interface chemistry, we find that Al_2O_3 after a high-temperature

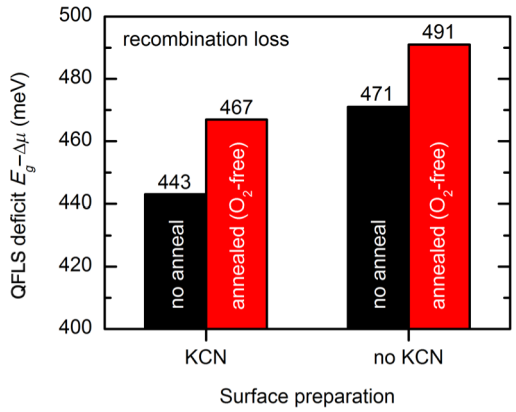

FIG. 7. Quasi-Fermi-level-splitting deficit $E_g - \Delta\mu$ obtained by calibrated PL for bare CIGS absorbers with or without etching in 5 wt-% KCN solution to remove surface oxides: before (black bars) and after (red bars) annealing for 2.5 min at 350 °C in 800 mbar of nitrogen gas in an RTP furnace. In both cases, recombination losses increase with annealing. Note that absolute values of QFLS deficit are not comparable to values shown for passivated absorbers, because the absorber—although with nominally similar composition—is from a different deposition run.

(350 °C) anneal stands out as providing the best level of surface passivation of all approaches investigated here. After a low temperature anneal at 150 °C, on the other hand, Al_2O_3 with a QFLS deficit around 460 meV is again very similar to these alternatives. The reason for this trend is an additional beneficial field-effect passivation due to the formation of negative fixed charges in the Al_2O_3 passivation layer. There is very little evidence to identify where exactly fixed charges are located in Al_2O_3-passivated CIGS, but nevertheless, changes in interface chemistry during annealing will impact formation and stability of the field-effect passivation.

Two different mechanisms have been proposed to explain the negative fixed-charge density in Al_2O_3 deposited on *c*-Si: (i) accumulation of tetrahedrally coordinated AlO_4^- (compared to octahedral Al_3^+) near the Al_2O_3/c-Si interface, induced by tetrahedrally coordinated Si in a thin interfacial SiO_x interlayer [65,66], and (ii) charged intrinsic point defects inside the Al_2O_3 layer [67–69]. Indeed, the Al_2O_3/c-Si interface-charge density can be manipulated by illumination with high-energy photons [70,71] or by applying a reverse bias voltage [72], which is explained by electron injection into such defect levels inside the Al_2O_3. These structural and electronic properties are very specific for each material, and it is reasonable to assume that Al_2O_3 in this regard will behave differently from other dielectric passivation layers. In Refs. [34,72] we have provided a summary of the relation between fixed charge, electronic defect levels, and chemical composition within Al_2O_3 deposited on *c*-Si. The very stable fixed-charge density of -4×10^{12} cm^{-2} in the Al_2O_3/c-Si system is consistently attributed to *oxygen-rich* Al_2O_3 due to the high amount of excess oxygen at the interface [34,73]. The rough surface of polycrystalline CIGS makes accurate quantification of the oxygen content within the Al_2O_3 very challenging, but we would expect *oxygen-poor* Al_2O_3 near the interface because the passivation layer serves as oxygen source for a substantial interfacial oxidation during annealing. The magnitude of the fixed-charge density $Q_f = -(2 \pm 1) \times 10^{12}$ cm^{-2} we determine in Sec. III for Al_2O_3/CIGS is indeed somewhat lower than usually reported for Al_2O_3/c-Si.

A potential origin of the negative charge in oxygen-poor Al_2O_3 could then be electron injection from CIGS into aluminum dangling bonds [68] within the Al_2O_3. This has been already observed for Al_2O_3/c-Si, where (i) an increase in fixed-charge density upon biasing [72] is consistent with the energy level of the Al dangling bond close to the Si conduction band edge [68], and (ii) trapping of electrons in Al_2O_3 was found to be much faster than detrapping after annealing [70]. Even if the fixed charges are likely located inside the Al_2O_3 alone, a high-bandgap "spacer layer" between Al_2O_3 and CIGS bulk (i.e., the oxidized surface) is essential to maintain a high and stable fixed-charge density. Without such a spacer layer, relaxation processes of the native point defects inside the Al_2O_3, origin of at least part of the fixed-charge density, is much faster, resulting in a low equilibrium net charge density.

This proposed model has a strong impact on field-effect passivation in CIGS solar cells and its long-term stability: in contrast to the tetrahedral coordination near the interface and deep trap levels related to oxygen, which give rise to the stable fixed charge in Al_2O_3/c-Si, the Al-related trap levels important for Al_2O_3/CIGS are expected to lie above the Fermi level in CIGS solar cells. Their charge state is susceptible to external influences, e.g., illumination, bias voltage, or temperature, which enhance detrapping mechanisms of the negative fixed charge. Indeed, unlike for Al_2O_3/c-Si, we often observe hysteresis effects—and thus instabilities in the fixed-charge density—in capacitance-voltage measurements of Al_2O_3/CIGS *M-I-S* devices. For the devices investigated here, the hysteresis in the flat-band voltage is up to 600 mV (see Fig. S4 within the Supplemental Material [45]), corresponding to a difference of up to approximately 10^{12} cm^{-2} in the apparent fixed-charge density. We propose that such hysteresis effects are likely universal for the field-effect passivation of CIGS surfaces, because the oxidized CIGS surface is a less efficient spacer layer than, for example, a high-bandgap SiO_2 in Al_2O_3/c-Si devices.

D. Bulk degradation caused by oxide-based passivation layers

Voltage-dependent admittance spectroscopy in Fig. 2 revealed a bulklike defect level around 150–200 meV,

which initially is hidden behind the large capacitive contribution of the interface states. It might be no coincidence that a very similar defect level with activation energy around 200 meV is commonly observed in CIGS grown under Cu excess ("Cu rich"), and found to be one of the root causes for increased interface recombination in Cu-rich devices [74]. Such a 200 meV defect in Cu-rich absorbers appears to be related to a near-surface Se deficiency caused by the highly oxidizing KCN etching, which is necessary to remove detrimental Cu_xSe secondary phases for Cu-rich growth conditions [74,75]. As we show in Sec. IV, a similar oxidation of Se species occurs also during an annealing process involving an oxide-based passivation layer. In our test devices investigated here, such a defect level plays no major role, as evidenced by the excellent low QFLS values achieved with oxide passivation layers. In a full front-passivated device, however, tunneling enhanced recombination via such surface-near defect states—similar to limitations found in Cu-rich solar cells—could partly negate the benefits of interface passivation.

A further challenge for integration of dielectric passivation layers into standard thin-film solar-cell fabrication processes arises from the finite thermal stability of these oxide layers: in our experiments we observe a noticeable degradation of QFLS and effective lifetime for annealing at temperatures exceeding 200 °C already for a few minutes. We attribute this deterioration mostly to the bulk-like defect level around 150–200 meV discussed above, which becomes increasingly prevalent after exposing the absorber to a higher thermal budget. Although our annealing conditions (N_2 background pressure in a low-vacuum RTP) are different from standard growth conditions (high Se flux in an ultrahigh vacuum chamber), such stability issues must be considered in process development.

VI. PROOF-OF-CONCEPT DEMONSTRATION OF A FULL-AREA REAR-INTERFACE PASSIVATION SCHEME

Industrial exploitation of dielectric passivation layers, which are typically insulating, requires a scalable and cost-efficient patterning technology to fabricate contact openings in the insulating passivation layer. The small grain size and low diffusion length in CIGS, both in the range of a few micrometers at most, thus require contact openings with diameters and spacing of a few tens to hundreds of nanometers [35–37,76]. As we show in Fig. 6, the interesting region defining interface chemistry—and which thus determines the level of chemical interface passivation—only extends over a depth of a few nanometers into the CIGS absorber. This opens up the possibility of making the passivation layer thin enough to still fully passivate defects at the respective interface, while being conductive enough to support a high photocurrent density even across a full-area dielectric layer without any contact openings. Although Al_2O_3 is an ideal choice for the rear-side passivation of p-type CIGS solar-cell absorbers due to the additional benefit of field-effect passivation, its high resistivity demands a delicate compromise between resistance (thin layer) and stability during absorber deposition (thick layer). We attempt to process a full-area back-side passivation with Al_2O_3 layers. However, if the layer is too thick, current transport through the back contact is hampered and we cannot obtain any photocurrent. Thin Al_2O_3 layers of only a few monolayers thickness are dissolved into the absorber during the rather long absorber deposition process on the order of an hour at temperatures above 500 °C. In that case, the solar-cell parameters are essentially identical to an unpassivated Mo back contact. We believe that an optimization is possible, although it would be time consuming and an acceptable process window might be small. A simpler solution appears to be using a more conductive passivation layer, giving a greater freedom over the choice of passivation-layer thickness.

Here we focus on a full-area rear-passivation layer of 3 nm of TiO_2 deposited by thermal ALD onto Mo-coated SLG substrates as a proof-of-concept device based on chemical passivation alone. We find that TiO_2 is more conductive than Al_2O_3, which means that the precise control of passivation-layer thickness becomes less critical for the solar cell.

Recombination at the rear Mo/CIGS interface is most detrimental for thin absorber layers without a Ga back gradient [16], which itself already passivates the rear interface (albeit at the cost of reduced absorption due to the higher bandgap). Such thin devices with low Ga content are particularly desirable for future high-efficiency CIGS solar cells, because thin absorbers save precious raw materials, and lower Ga content increases absorption and limits the impact of detrimental Ga-related defects. Accordingly, we use a 1.1 ± 0.2-μm-thick Cu-poor absorber grown in a single-stage process without Ga gradient (Cu content CGI = 0.80, Ga content GGI = 0.33), which is more relevant for potential applications of rear-passivation layers than a standard 2-μm-thick double-graded absorber. Note that our deposition process is not optimized for these conditions, resulting in fairly small-grained material (average grain diameter approximately 500 nm) with low PL yield. We also do not use any alkali postdeposition processing or antireflection coatings, because their optimization for different back-contact configurations is outside the scope of this paper. Unpassivated reference solar cells with Mo/CIGS rear interface achieve efficiency values of 13.6%–14.2% (four devices, average 13.8%). The best device is shown by the black line in Fig. 8.

Solar cells with a full-area TiO_2 rear-passivation layer improve in open-circuit voltage V_{OC} (from 657 ± 4 mV to 674 ± 4 mV, +17 mV) and short-circuit current density J_{SC}, (from 29.3 ± 0.8 mA/cm^2 to 31.5 ± 0.5 mA/cm^2,

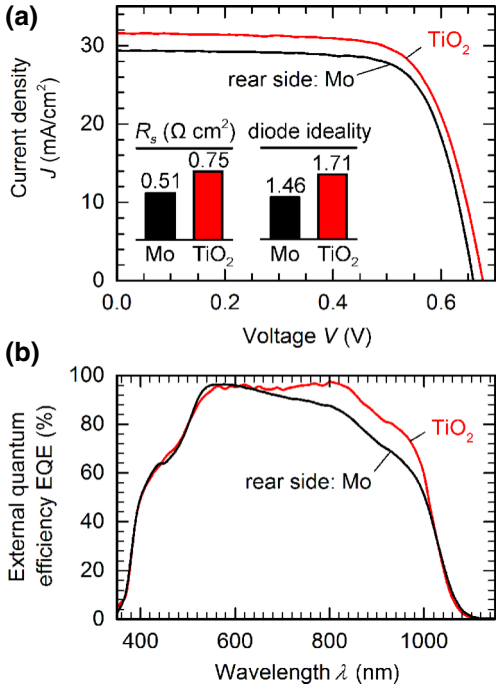

FIG. 8. Full-area rear-passivated CIGS solar cells. (a) Illuminated current density–voltage (J-V) characteristics of the best thin solar cells with standard Mo back contact (black line) and with 3-nm TiO_2 passivation layer (red line) after storage in vacuum (solid lines). The insets show series resistance R_s (scale 0–1 Ωcm^2) and diode ideality factor (scale 1–2) obtained from the dark J-V curves. (b) External quantum efficiency of the reference and passivated devices showing the improvement in long-wavelength response for the passivated device.

$+2.2$ mA/cm^2) compared to the Mo references, but suffer from reduced fill factor FF (from $72\% \pm 2\%$ down to $67 \pm 3\%$). As a result, full-area rear-passivated solar cells reached efficiencies between 14.0%–15.3%, compared to 13.6%–14.2% of the reference devices. The large spread in efficiency for the passivated devices is mostly due to the different fill factors.

The best rear-passivated solar cell reaches an efficiency of 15.3% (red line in Fig. 8), a gain of more than 1% absolute in efficiency compared to the best unpassivated reference device. Note that these values are measured after storage in vacuum and that these differences are less pronounced directly after processing. This efficiency boost after aging is stable over long time periods: after 6 months of storage in an evacuated plastic bag, the efficiencies remained essentially stable (15.1% for the TiO_2-passivated solar cell presented above).

Compared to record devices around 23% [10,12], the present result might appear low. This is largely explained by the thinner absorber layer and a lack of bandgap gradient, alkali treatment, and antireflection coating. Note, that an efficiency above 15% is the highest reported so far for rear-passivated solar cells below 1.5 μm thickness [32]. Concerning the benefit of a rear-passivation layer, we find that the gain in J_{SC} originates from a significant enhancement of the long-wavelength response evident from the difference in external quantum efficiency shown in Fig. 8(b), which is in agreement with a reduction of recombination losses at the rear of the device. The improvement of $+17$ mV in V_{OC} is close to the difference in QFLS of $+22$ meV of the different absorbers covered with CdS. Surprisingly, the reduced FF in passivated devices is mostly driven by a higher diode ideality factor, although series resistance is higher in the passivated devices as well, as shown in the inset of Fig. 8(a). A possible explanation for the increased ideality factor in passivated devices might be a shift of the dominant recombination channel towards the front of the device: as we suppress recombination at the rear interface or deep within the quasineutral bulk near that rear interface, nonradiative recombination will be increasingly dominated by recombination channels within the space-charge region at the front of the device, which ideally can be described by an ideality factor close to 2.

Obviously, it is of great importance that the thin passivation layer at the rear contact is not destroyed by the absorber deposition process. Solar-cell parameters and photoluminescence measurements clearly indicate that the TiO_2 layer passivating the back contact in the solar cells presented above indeed survives the cell fabrication process: the high series resistance of rear-passivated solar cells exceeds all reasonable limits below 0.6 Ωcm^2 for solar cells with Mo back contact, thus confirming the presence of a blocking layer. The significant increase in diode ideality factor in rear-passivated solar cells is also best explained by a change in recombination at the back contact. The optical diode factor in excitation-dependent PL measurements follows the same trend (see Fig. S5 within the Supplemental Material [45]), confirming that devices with a TiO_2-passivated back contact behave similar to devices with intact rear-passivation layer, and clearly differ from unpassivated references. Furthermore, both QFLS and V_{OC} improve, confirming lower recombination losses and indicating that the absorber growth process effectively replaces a thermal postdeposition annealing. Compared to the unpassivated Mo back contact, the QFLS improves by $+22$ meV with 3 nm of TiO_2 and $+32$ meV with 20 nm of Al_2O_3, which appears reasonable considering the additional field-effect passivation for Al_2O_3 [compare Fig. 6(b)]. There is no doubt that a 20-nm-thick Al_2O_3 layer survives the absorber deposition: the series resistance in these cells exceeds 100 Ωcm and the photocurrent is effectively suppressed. In contrast, for ultrathin passivation layers of only a few monolayers of Al_2O_3 we measure solar-cell characteristics identical to Mo/CIGS reference devices, indicating that too thin layers are indeed destroyed during the growth process.

VII. CONCLUSIONS

We deposit metal-oxide (Al_2O_3 and TiO_2) passivation layers by ALD onto CIGS surfaces to effectively suppress interface recombination in thin-film solar cells. The ALD process on CIGS resulted in highly defective interfaces with interface trap densities above 10^{12} eV^{-1} cm^{-2} and low effective lifetimes of a few nanoseconds. Postdeposition thermal annealing in nitrogen leads to a marked improvement in interface passivation: the interface trap density decreased significantly, leading to an increase in effective lifetime and quasi-Fermi-level splitting. At annealing temperatures around 350 °C we confirm the formation of negative fixed charges at the Al_2O_3/CIGS interface, leading to a pronounced field-effect passivation further suppressing recombination losses.

The annealing process causes an accumulation of mobile Na at the interface between CIGS and passivation layer, and at the same time promotes the oxidation of near-interface CIGS due to the presence of oxygen in the passivation layer. At sufficiently high temperatures Cu and Se are depleted from the interface, leading to the formation of an indium-gallium-oxide interfacial layer. This interface oxidation upon annealing can be exploited to passivate the CIGS surface independent of the specific choice of passivation layer: annealing a CIGS thin film exposed to an oxygen plasma, we are able to achieve a surface passivation quality comparable to that of a state-of-the-art CdS buffer layer. As a further consequence, different oxide-based passivation approaches showed the same electronic quality with respect to chemical passivation, with Al_2O_3 achieving superior performance due to the additional field-effect passivation.

While we find striking similarities between CIGS and *c*-Si solar cells—for example, concerning interface damage during ALD and interlayer formation—the detailed chemical processes and their reaction rates are very different between these two technologies. Accordingly, care must be taken in the transfer of know-how from *c*-Si technology to thin-film solar cells. We find that this will particularly affect the formation of negative fixed charges and the thermal stability of the passivated interface.

We present a simple prototype for a thin ungraded solar cell with a TiO_2 full-area rear-interface passivation layer, which does not require any contact patterning and achieves more than 1% absolute efficiency gain compared to a standard Mo/CIGS back-contact design.

ACKNOWLEDGMENTS

We thank M. Melchiorre, M. Sood, and F. Ehre (University of Luxembourg) for assistance with chemical etching and N. Valle and B. El Adib (Luxembourg Institute of Science and Technology) for SIMS measurements. This study is funded by the Fonds National de la Recherche Luxembourg in the project "Surface passivation for thin film photovoltaics (SURPASS)."

F.W. coordinated the research, performed electrical characterization and annealing, and wrote the manuscript. B.V.-W. deposited the passivation layers, C.S. and M.R.B. carried out PL characterization, F.B. deposited CIGS absorbers, J.G. performed XPS characterization. J.S. and Su.S. provided scientific support. All authors contributed to data interpretation and planning experiments.

The authors declare no competing interests.

[1] M. A. Green, Y. Hishikawa, E. D. Dunlop, D. H. Levi, J. Hohl-Ebinger, M. Yoshita, and A. W. Y. Ho-Baillie, Solar cell efficiency tables (version 53), Prog. Photovolt **27**, 3 (2019).

[2] K. Zweibel, Thin films: Past, present, future, Prog. Photovolt **3**, 279 (1995).

[3] J. Peng, L. Lu, and H. Yang, Review on life cycle assessment of energy payback and greenhouse gas emission of solar photovoltaic systems, Renew. Sust. Energ. Rev. **19**, 255 (2013).

[4] M. J. de Wild-Scholten, Energy payback time and carbon footprint of commercial photovoltaic systems, Sol. Energ. Mat. Sol. C **119**, 296 (2013).

[5] E. G. Hertwich, J. A. de Larderel, A. Arvesen, P. Bayer, J. Bergesen, E. Bouman, T. Gibon, G. Heath, C. Peña, P. Purohit, A. Ramirez, and S. Suh (eds). *Green Energy Choices: The Benefits, Risks and Trade-Offs of low-Carbon Technologies for Electricity Production* (Report of the International Resource Panel. UNEP, 2016).

[6] U. Rau and H. W. Schock, Electronic properties of $Cu(In, Ga)Se_2$ heterojunction solar cells - recent achievements, current understanding, and future challenges, Appl. Phys. A **69**, 131 (1999).

[7] R. Scheer and H. W. Schock, *Chalcogenide Photovoltaics: Physics, Technologies, and Thin Film Devices* (Wiley-VCH, Weinheim, Germany, 2011).

[8] W. N. Shafarman, S. Siebentritt, and L. Stolt, $Cu(In, Ga)Se_2$ *Solar Cells* (Wiley and Sons, Chichester, UK, 2011), 2nd edn.

[9] R. Carron, S. Nishiwaki, T. Feurer, R. Hertwig, E. Avancini, J. Löckinger, S.-C. Yang, S. Buecheler, and A. N. Tiwari, Advanced alkali treatments for high-efficiency $Cu(In, Ga)Se_2$ solar cells on flexible substrates, Adv. Energy. Mater. **9**, 1900408 (2019).

[10] P. Jackson, R. Wuerz, D. Hariskos, E. Lotter, W. Witte, and M. Powalla, Effects of heavy alkali elements in Cu(In, Ga)Se2 solar cells with efficiencies up to 22.6%, Phys. Status Solidi (RRL) **10**, 583 (2016).

[11] Solar Frontier. Solar frontier achieves world record thin-film solar cell efficiency of 23.35% (2019). http:/www.solar-frontier.com/eng/news/2019/0117_press.html.

[12] M. Nakamura, K. Yamaguchi, Y. Kimoto, Y. Yasaki, T. Kato, and H. Sugimoto, Cd-free $Cu(In, Ga)(Se, S)_2$ thin-film solar cell with a new world record efficacy of 23.35%, IEEE J. Photovolt **9**, 1863 (2018).

[13] S. Rühle, Tabulated values of the Shockley-Queisser limit for single junction solar cells, Sol. Energy **130**, 139 (2016).

[14] W. Shockley and H. J. Queisser, Detailed balance limit of efficiency of p-n junction solar cells, J. Appl. Phys. **32**, 510 (1961).

[15] S. Siebentritt, What limits the efficiency of chalcopyrite solar cells?, Sol. Energ. Mat. Sol. C **95**, 1471 (2011).

[16] T. P. Weiss, B. Bissig, T. Feurer, R. Carron, S. Buecheler, and A. N. Tiwari, Bulk and surface recombination properties in thin film semiconductors with different surface treatments from time-resolved photoluminescence measurements, Sci. Rep. **9**, 5385 (2019).

[17] J. A. van Delft, D. Garcia-Alonso, and W. M. M. Kessels, Atomic layer deposition for photovoltaics: Applications and prospects for solar cell manufacturing, semicond, Sci. Tech. **27**, 074002 (2012).

[18] T. Dullweber and J. Schmidt, Industrial silicon solar cells applying the passivated emitter and rear cell (PERC) concept - A review, IEEE J. Photovolt **6**, 1366 (2016).

[19] J. Schmidt, R. Peibst, and R. Brendel, Surface passivation of crystalline silicon solar cells: Present and future, Sol. Energ. Mat. Sol. C **187**, 39 (2018).

[20] W.-W. Hsu, J. Y. Chen, T.-H. Cheng, S. C. Lu, W.-S. Ho, Y.-Y. Chen, Y.-J. Chien, and C. W. Liu, Surface passivation of $Cu(In, Ga)Se_2$ using atomic layer deposited Al_2O_3, Appl. Phys. Lett. **100**, 023508 (2012).

[21] B. Vermang, V. Fjällström, J. Pettersson, P. Salome, and M. Edoff, Development of rear surface passivated $Cu(In, Ga)Se_2$ thin film solar cells with nano-sized local rear point contacts, Sol. Energ. Mat. Sol. C. **117**, 505 (2013).

[22] B. Vermang, J. T. Wätjen, V. Fjällström, F. Rostvall, M. Edoff, R. Kotipalli, F. Henry, and D. Flandre, Employing Si solar cell technology to increase efficiency of ultra-thin $Cu(In, Ga)Se_2$ solar cells, Prog. Photovolt. **22**, 1023 (2014).

[23] B. Vermang, J. T. Wätjen, C. Frisk, V. Fjällström, F. Rostvall, M. Edoff, P. Salomé, J. Borme, N. Nicoara, and S. Sadewasser, Introduction of Si PERC rear contacting design to boost efficiency of $Cu(In, Ga)Se_2$ solar cells, IEEE J. Photovolt. **4**, 1644 (2014).

[24] T. Suntola and J. Antson, Method for producing compound thin films, U.S. Patent 40584301977 (1977).

[25] G. Agostinelli, A. Delabie, P. Vitanov, Z. Alexieva, H. F. W. Dekkers, S. D. Wolf, and G. Beaucarne, Very low surface recombination velocities on p-type silicon wafers passivated with a dielectric with fixed negative charge, Sol. Energ. Mat. Sol. C **90**, 3438 (2006).

[26] B. Hoex, S. B. S. Heil, E. Langereis, M. C. M. van de Sanden, and W. M. M. Kessels, Ultralow surface recombination of c-Si substrates passivated by plasma-assisted atomic layer deposited Al_2O_3, Appl. Phys. Lett. **89**, 042112 (2006).

[27] K. Jaeger and R. Hezel, in *Proceedings of the 18th IEEE Photovoltaic Specialists Conference* (1985), pp. 1752–1753.

[28] J. Schmidt, A. Merkle, R. Brendel, B. Hoex, M. C. M. van de Sanden, and W. M. M. Kessels, Surface passivation of high-efficiency silicon solar cells by atomic-layer-deposited Al_2O_3, Prog. Photovolt **16**, 461 (2008).

[29] G. Dingemans, M. C. M. van de Sanden, and W. M. M. Kessels, Influence of the deposition temperature on the c-Si surface passivation by Al_2O_3 films synthesized by ALD and PECVD, Electrochem. Solid St. **13**, 76 (2010).

[30] P. Saint-Cast, D. Kania, M. Hofmann, J. Benick, J. Rentsch, and R. Preu, Very low surface recombination velocity on p-type c-Si by high-rate plasma-deposited aluminum oxide, Appl. Phys. Lett. **95**, 151502 (2009).

[31] T.-T. Li and A. Cuevas, Effective surface passivation of crystalline silicon by rf sputtered aluminum oxide, Phys. Status Solidi (RRL) **3**, 160 (2009).

[32] G. Birant, J. de Wild, M. Meuris, J. Poortmans, and B. Vermang, Dielectric-Based rear surface passivation approaches for Cu(In, Ga)Se2 solar cells-A review, Appl. Sci. **9**, 677 (2019), and references therein.

[33] J. Keller, F. Gustavsson, L. Stolt, M. Edoff, and T. Törndahl, On the beneficial effect of Al2O3 front contact passivation in Cu(In, Ga)Se2 solar cells, Sol. Energ. Mat. Sol. C. **159**, 189 (2017).

[34] F. Werner, B. Veith, D. Zielke, L. Kühnemund, C. Tegenkamp, M. Seibt, R. Brendel, and J. Schmidt, Electronic and chemical properties of the c-Si/Al_2O_3 interface, J. Appl. Phys. **109**, 113701 (2011).

[35] N. Allsop, R. Nürnberg, M. C. Lux-Steiner, and T. Schedel-Niedrig, Three-dimensional simulations of a thin film heterojunction solar cell with a point contact/defect passivation structure at the heterointerface, Appl. Phys. Lett. **95**, 122108 (2009).

[36] A. Bercegol, B. Chacko, R. Klenk, I. Lauermann, M. C. Lux-Steiner, and M. Liero, Point contacts at the copper-indium-gallium-selenide interface—A theoretical outlook, J. Appl. Phys. **119**, 155304 (2016).

[37] G. Sozzi, S. D. Napoli, R. Menozzi, B. Bissig, S. Buecheler, and A. N. Tiwari, Impact of front-side point contact/passivation geometry on thin-film solar cell performance, Sol. Energ. Mat. Sol. C **165**, 94 (2017).

[38] A. Richter, J. Benick, M. Hermle, and S. W. Glunz, Reaction kinetics during the thermal activation of the silicon surface passivation with atomic layer deposited Al_2O_3, Appl. Phys. Lett. **104**, 061606 (2014).

[39] G. Dingemans, N. M. Terlinden, D. Pierreux, H. B. Profijt, M. C. M. van de Sanden, and W. M. M. Kessels, Influence of the oxidant on the chemical and field-effect passivation of Si by ALD Al_2O_3, Electrochem. Solid St. **14**, H1 (2011).

[40] F. Werner, B. Veith, V. Tiba, P. Poodt, F. Roozeboom, R. Brendel, and J. Schmidt, Very low surface recombination velocities on p- and n-type c-Si by ultrafast spatial atomic layer deposition of aluminum oxide, Appl. Phys. Lett. **97**, 162103 (2010).

[41] R. Kotipalli, B. Vermang, J. Joel, R. Rajkumar, M. Edoff, and D. Flandre, Investigating the electronic properties of Al_2O_3/$Cu(In, Ga)Se_2$ interface, AIP Adv. **5**, 107101 (2015).

[42] T. Unold and L. Gütay, *Photoluminescence Analysis of Thin-Film Solar Cells, in Advanced Characterization Techniques for Thin Film Solar Cells* (Wiley-VCH, Weinheim, Germany, 2011).

[43] P. Blood and J. W. Orton, *The Electrical Characterization of Semiconductors: Majority Carriers and Electron States* (Academic Press, London, 1992).

[44] E. H. Nicollian and J. R. Brews, *MOS (Metal Oxide Semiconductor) Physics and Technology* (Wiley, New York, 1982).

[45] See Supplemental Material at http://link.aps.org/supplemental/10.1103/PhysRevApplied.13.054004 for (a) further capacitance spectra, (b) comparison of simulation parameters with independent measurements, (c) relation between flatband voltage and fixed-charge density, (d) XPS results for Cu and K, (e) interface defects with alternative ALD process, (f) hysteresis in *CV* measurements, and (g) optical ideality factor of rear-passivated solar cells.

[46] F. Werner, B. Veith-Wolf, M. Melchiorre, F. Babbe, J. Schmidt, and S. Siebentritt, Ultra-thin passivation layers in $Cu(In, Ga)Se_2$ thin-film solar cells: Full-area passivated front contacts and their impact on bulk absorber doping, Sci. Rep. (in press 2020).

[47] F. Werner, Hall measurements on low-mobility thin films, J. Appl. Phys. **122**, 135306 (2017).

[48] F. Werner, F. Babbe, J. Burkhart, C. Spindler, H. Elanzeery, and S. Siebentritt, Interdiffusion and doping gradients at the buffer/absorber interface in thin-film solar cells, ACS Appl. Mater. Inter. **10**, 28553 (2018).

[49] F. Werner, T. Bertram, J. Mengozzi, and S. Siebentritt, What is the dopant concentration in polycrystalline thin-film $Cu(In, Ga)Se_2$?, Thin Solid Films **633**, 222 (2017).

[50] F. Werner, Dissertation, Gottfried Wilhelm Leibniz Universität Hannover, 2014. Available online at http://edok01.tib.uni-hannover.de/edoks/e01dh14/799320552.pdf.

[51] J. Hedstrom, H. Ohlsen, M. Bodegard, A. Kylner, L. Stolt, D. Hariskos, M. Ruckh, and H. W. Schock, in *Conference Record of the IEEE Photovoltaic Specialists Conference* (1993), pp. 364–371.

[52] F. Pianezzi, P. Reinhard, A. Chirila, B. Bissig, S. Nishiwaki, S. Buecheler, and A. N. Tiwari, Unveiling the effects of post-deposition treatment with different alkaline elements on the electronic properties of CIGS thin film solar cells, Phys. Chem. Chem. Phys. **16**, 8843 (2014).

[53] D. Rudmann, D. Bremaud, H. Zogg, and A. N. Tiwari, Na incorporation into $Cu(In, Ga)Se_2$ for high-efficiency flexible solar cells on polymer foils, J. Appl. Phys. **97**, 084903 (2005).

[54] L. Kronik, D. Cahen, and H. W. Schock, Effects of sodium on polycrystalline Cu(In, Ga)Se2 and Its solar cell performance, Adv. Mater. **10**, 31 (1998).

[55] J. F. Moulder, W. F. Stickle, P. E. Sobol, and K. D. Bomben, *Handbook of X-Ray Photoelectron Spectroscopy* (Perkin-Elmer, Eden Prairie, USA, 1992).

[56] G. Dingemans, W. Beyer, M. C. M. van de Sanden, and W. M. M. Kessels, Hydrogen induced passivation of Si interfaces by Al_2O_3 films and SiO_2/Al_2O_3 stacks, Appl. Phys. Lett. **97**, 152106 (2010).

[57] D. Cahen, P. J. Ireland, L. L. Kazmerski, and F. A. Thiel, X-ray photoelectron and auger electron spectroscopic analysis of surface treatments and electrochemical decomposition of CuInSe2 photoelectrodes, J. Appl. Phys. **57**, 4761 (1985).

[58] E. Niemi and L. Stolt, Characterization of $CuInSe_2$ thin films by XPS, Surf. Interface Anal. **15**, 422 (1990).

[59] U. Rau, D. Braunger, R. Herberholz, H. W. Schock, J.-F. Guillemoles, L. Kronik, and D. Cahen, Oxygenation and air-annealing effects on the electronic properties of $Cu(In, Ga)Se_2$ films and devices, J. Appl. Phys. **86**, 497 (1999).

[60] J. L. Bourque, M. C. Biesinger, and K. M. Baines, Chemical state determination of molecular gallium compounds using XPS, Dalton Trans. **45**, 7678 (2016).

[61] E. Handick, P. Reinhard, R. G. Wilks, F. Pianezzi, T. Kunze, D. Kreikemeyer-Lorenzo, L. Weinhardt, M. Blum, W. Yang, M. Gorgoi, E. Ikenaga, D. Gerlach, S. Ueda, Y. Yamashita, T. Chikyow, C. Heske, S. Buecheler, A. N. Tiwari, and M. Bär, Formation of a K-In-Se surface species by NaF/KF postdeposition treatment of $Cu(In, Ga)Se_2$ thin-film solar cell absorbers, ACS Appl. Mater. Inter. **9**, 3581 (2017).

[62] D. Hauschild, F. Meyer, S. Pohlner, R. Lechner, R. Dietmüller, J. Palm, C. Heske, L. Weinhardt, and F. Reinert, Impact of environmental conditions on the chemical surface properties of $Cu(In, Ga)(S, Se)_2$ thin-film solar cell absorbers, J. Appl. Phys. **115**, 183707 (2014), and references therein.

[63] D. Regesch, L. Gütay, J. K. Larsen, V. Deprédurand, D. Tanaka, Y. Aida, and S. Siebentritt, Degradation and passivation of $CuInSe_2$, Appl. Phys. Lett. **101**, 112108 (2012), and references therein.

[64] R. Würz, A. Meeder, D. F. Marron, T. Schedel-Niedrig, and K. Lips, An electron paramagnetic resonance and photoelectron spectroscopy study on the native oxidation of $CuGaSe_2$, Mater. Res. Soc. Symp. Proc. **865**, F5.36.1 (2005), and references therein.

[65] K. Kimoto, Y. Matsui, T. Nabatame, T. Yasuda, T. Mizoguchi, I. Tanaka, and A. Toriumi, Coordination and interface analysis of atomic-layer-deposition Al_2O_3 on Si(001) using energy-loss near-edge structures, Appl. Phys. Lett. **83**, 4306 (2003).

[66] G. Lucovsky, A chemical bonding model for the native oxides of the III–V compound semiconductors, J. Vac. Sci. Technol. **19**, 456 (1981).

[67] K. Matsunaga, T. Tanaka, T. Yamamoto, and Y. Ikuhara, First-principles calculations of intrinsic defects in Al_2O_3, Phys. Rev. B **68**, 085110 (2003).

[68] B. Shin, J. R. Weber, R. D. Long, P. K. Hurley, C. G. Van de Walle, and P. C. McIntyre, Origin and passivation of fixed charge in atomic layer deposited aluminum oxide gate insulators on chemically treated InGaAs substrates, Appl. Phys. Lett. **96**, 152908 (2010).

[69] J. R. Weber, A. Janotti, and C. G. Van de Walle, Native defects in Al_2O_3 and their impact on III-V/Al_2O_3 metal-oxide-semiconductor-based devices, J. Appl. Phys. **109**, 033715 (2011).

[70] J. J. H. Gielis, B. Hoex, M. C. M. van de Sanden, and W. M. M. Kessels, Negative charge and charging dynamics in Al_2O_3 films on Si characterized by second-harmonic generation, J. Appl. Phys. **104**, 073701 (2008).

[71] B. Liao, R. Stangl, T. Mueller, F. Lin, C. S. Bhatia, and B. Hoex, The effect of light soaking on crystalline silicon surface passivation by atomic layer deposited Al_2O_3, J. Appl. Phys. **113**, 024509 (2013).

[72] F. Werner and J. Schmidt, Manipulating the negative fixed charge density at the c-Si/Al_2O_3 interface, Appl. Phys. Lett. **104**, 091604 (2014).

[73] V. Naumann, M. Otto, R. B. Wehrspohn, and C. Hagendorf, Chemical and structural study of electrically passivating Al2O3/Si interfaces prepared by atomic layer deposition, J. Vac. Sci. Technol. A **30**, 04D106 (2012).

[74] H. Elanzeery, M. Melchiorre, M. Sood, F. Babbe, F. Werner, G. Brammertz, and S. Siebentritt, Challenge in Cu-rich $CuInSe_2$ thin film solar cells: Defect caused by etching, Phys. Rev. Mat. **3**, 055403 (2019).

[75] D. Colombara, H. Elanzeery, N. Nicoara, D. Sharma, M. Claro, T. Schwarz, A. Koprek, M. Wolter, N. Valle, O. Bondarchuk, M. Melchiorre, F. Babbe, C. Spindler, O. Cojocaru-Miredin, D. Raabe, P. J. Dale, S. Sadewasser, and S. Siebentritt, Chemical instability of chalcogenide surfaces near phase boundaries, Nat. Commun., in Revision (2019).

[76] B. Vermang, V. Fjällström, X. Gao, and M. Edoff, Improved rear surface passivation of $Cu(In, Ga)Se_2$ solar cells: A combination of an Al_2O_3 rear surface passivation layer and nanosized local rear point contacts, IEEE J. Photovolt. **4**, 486 (2014).